DOI: 10.31276/VJSTE.2024.0146


# Parameter optimisation for single-track laser cladding using the Taguchi-Grey relational approach

**Van Quan Nguyen, Tat Khoa Doan*, Van Nguy Duong, Van Hoang Nguyen**

*Faculty of Mechanical Engineering, Le Quy Don Technical University, 236 Hoang Quoc Viet Street, Nghia Do Ward, Hanoi, Vietnam*

Received 29 December 2024; revised 16 January 2025; accepted 16 October 2025

***Abstract:***

**The judicious selection of laser cladding (LC) process parameters is essential for the clad bead geometry. In this research, the Taguchi-Grey relational method was chosen to enhance the quality of single-track bead geometry and to perform multi-objective optimisation of process parameters. The Taguchi method was selected to construct an L16 orthogonal experiment. The impact of significant LC parameters (laser power (P), scanning speed (S), and powder feeding rate (F)) on the responses (width (W), height (H), penetration (Pene), and dilution rate) was analysed based on the analysis of variance (ANOVA). The findings indicated that the scanning speed was the most important factor affecting the ratio of layer W, H, Pene, and dilution rate of the cladding. Subsequently, grey relational analysis (GRA) was employed to consolidate the four response variables into a singular grey relational grade (GRG) for quantification and optimisation purposes. Finally, the optimum cladding process parameters were obtained. The face-centred cubic (FCC) single-phase coating was observed using X-ray diffraction (XRD), scanning electron microscopy (SEM), and energy dispersive spectroscopy (EDS) to analyse the microstructure and chemical composition of the coating. Moreover, hardness measurements exhibited a gradual increase from the substrate (197 HV) to the cladding layer (224 HV), attributed to the distribution of Cr and Mo, solid solution strengthening, and microstructural refinement, demonstrating improved mechanical performance.**

***Keywords:*** **direct laser metal deposition, laser cladding, SS316L, Taguchi-Grey relational analysis.**

***Classification numbers:*** **2.1, 2.3**

## 1. Introduction

Laser cladding is an advanced surface modification technology that enhances resistance to high temperatures, corrosion, and wear. Additionally, it is employed to repair damaged components affected by wear or corrosion and is often referred to as a form of additive manufacturing. It is also classified under direct laser metal deposition (DLMD) technology [1, 2]. This technology is extensively utilised in the automotive, aviation, and aerospace sectors, particularly for components exposed to seawater corrosion, as well as in various other industrial sectors due to its benefits, which include a low dilution rate, reliable metallurgical bonding, minimal heat-affected zone, and exceptional performance characteristics. There are two feeding methods for LC: powder or wire feeding, with the powder-based laser coating method being more frequently employed [3]. The advantages of the powder method include shallower penetration depth and improved surface quality. It is a common method in experimental studies and is particularly convenient for parts with complex geometries, especially when cladding multi-materials [4]. The LC process is influenced by numerous parameters, such as P, S, F, shielding gas flow rate, and laser spot diameter.

The LC process involves numerous processing parameters, making it crucial to use combined parameters to investigate the relationship between these combinations and the resulting quality of the formation. Recently, research has primarily focused on the influence of single or several parameters. However, due to the complexity of the LC process, optimising these processing parameters presents numerous challenges. Additionally, the relationship between these parameters and the coating quality is generally nonlinear, complicating the development of precise mathematical models. Among these approaches, the Taguchi method has demonstrated a nonlinear relationship between product quality characteristics and a combination of characteristic parameters, making it a cost-effective and high-quality engineering method. The Taguchi-Grey relational method has been extensively utilised for optimising the technological parameters of LC coatings on quality carbon steel S55C, demonstrating its effectiveness in enhancing process efficiency and coating performance [5]. Their findings revealed that the Grey relational value increased by 0.153282, indicating significant improvements in the morphologies and microstructure of the optimised cladding coatings. Recent advancements in process parameter optimisation have incorporated Taguchi-based

*Corresponding author: Email: doankhoactm@gmail.com

methodologies [5], GRA [6, 7], and evolutionary algorithms [3], primarily focusing on P, S, and F. These studies have demonstrated significant improvements in surface morphology, mechanical properties, and cladding efficiency [8]. The aim of these studies is to enhance surface morphology, improve mechanical properties, and increase cladding efficiency [9, 10]. Additionally, statistical techniques such as ANOVA are frequently employed to assess the significance of process parameters [11, 12]. Predictive frameworks, including regression analysis and machine learning methods, have been developed to link process parameters with output characteristics [9, 13]. The optimisation strategies outlined in these studies have demonstrated notable improvements in cladding layer quality and process efficiency across various materials and applications. Despite these advancements, current optimisation studies have primarily neglected the phase composition and microstructural evolution at the interface between the substrate and the deposition layer. This represents a significant research deficiency, as the establishment of a robust metallurgical bond is essential for ensuring structural integrity, wear resistance, and long-term durability of the cladding layers. To address this limitation, the present study employs an advanced Taguchi-Grey methodology for multi-objective process optimisation, aiming to bridge the existing research voids and further enhance coating quality and operational efficiency in LC applications. Stainless steel 316L (SS316L) is exceptionally suitable for LC in parts repair and fabrication due to its corrosion resistance and improved hardness and wear resistance for rail repair, tooling, and high-load applications [11].

This paper employs the design of experiments (DOE) L16 using the Taguchi approach to establish a statistical relationship between process parameters (P, S, F) and responses (dilution rate, width, height, and penetration) of the LC SS316L coating. Additionally, SEM and energy dispersive spectroscopy were utilised to analyse the microstructure and chemical composition of the coating. The microhardness from the substrate material to the deposited surface is examined and evaluated.

## 2. Materials and methods

### *2.1. Materials and the laser cladding system*

The LC system utilised in this study comprised a 6.0 kW laser, a powder feeder, a deposition nozzle, a three-axis computer numerical control mechanism, and an inert gas (argon) source integrated to protect the molten pool from oxidation during cladding (Fig. 1A). The scanning electron microscope and energy dispersive X-ray analysis of the morphology and elemental percentage composition of the SS316L powder are presented in Figs. 1B and 1C. Table 1 details the chemical composition, with particle sizes ranging from 15 to 45 μm and an average size of 19.774 μm (Fig. 1D).

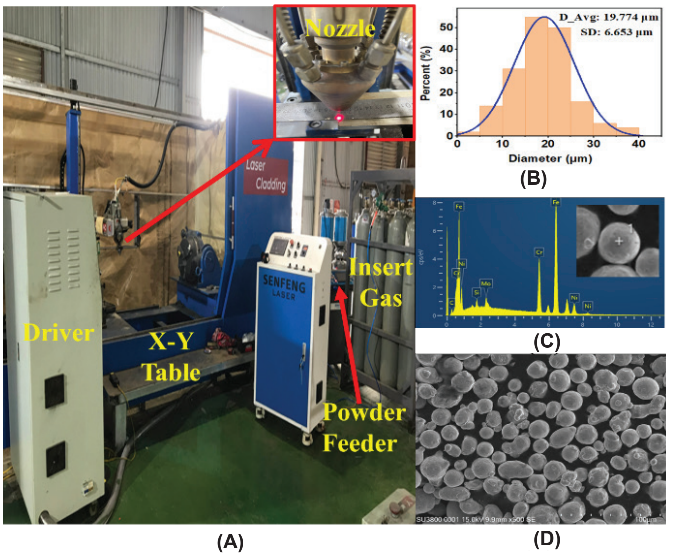


**Fig. 1. (A) The LC systems, (B) the powder size distribution, (C) EDS of 316L powder, (D) an SEM picture of the SS316L powder.**

In this work, SS316L plates with dimensions of 200x60x10 mm were employed as the substrate. Prior to coating, the substrates were sequentially polished and cleaned with acetone to remove grease and stains, thereby eliminating the surface oxidation layer and enhancing surface quality. The metal powder was dried in a vacuum oven at 120°C for 2 hours to remove moisture before LC.

**Table 1. Chemical composition of powder and substrate material (wt.%) SS316L.**

| SS316L | Cr (%) | Mo (%) | Ni (%) | Si (%) | Mn (%) | Fe (%) |
|---|---|---|---|---|---|---|
| Powder | 17.3 | 1.32 | 9.19 | 0.92 | 0.67 | Bal. |
| Substrate | 17.2 | 0.85 | 8.6 | 0.67 | 0.75 | Bal. |

### *2.2. Fabrication of samples and data collection*

In the LC process, numerous parameters can affect the quality and geometry of the tracks. These include the diameter of the laser beam point, the pressure and flow rate of the carrying/shielding gas, the particle size distribution, P, S, F, among others [7, 14, 15]. However, P, S, F are determined as the major factors that most substantially affect temperature distribution, melt pool dimensions, and track geometry [16]. Furthermore, changing certain parameters in the experiment is easier and more useful than changing others, such as the laser beam spot diameter or particle size distribution. Therefore, in this research, we focus on the parametric investigation and optimisation of P, S, F while keeping other parameters fixed at a constant value. The experimental strategy for fabricating the single deposited tracks was structured using the L16 orthogonal array Taguchi approach, incorporating four levels for each parameter, as detailed in Table 2.

**Table 2. Parameters and their levels utilised for LC.**

| Variables | Levels | | | |
|---|---|---|---|---|
| | *1* | *2* | *3* | *4* |
| P (W) | 1200 | 1500 | 1800 | 2100 |
| S (mm/min) | 800 | 900 | 1000 | 1100 |
| F (g/min) | 12 | 14 | 16 | 18 |

This resulted in a total of 16 experimental trials. The well-formed single tracks were deposited and subsequently cleaned, as shown in Fig. 2A. All depositions were performed using an intermittent coaxial nozzle with argon as the shielding gas. The shielding and carrying gas flow rates were maintained at 8 l/min. The distance from the nozzle to the substrate surface was fixed at 15 mm, and the laser beam spot diameter was controlled at 3 mm.

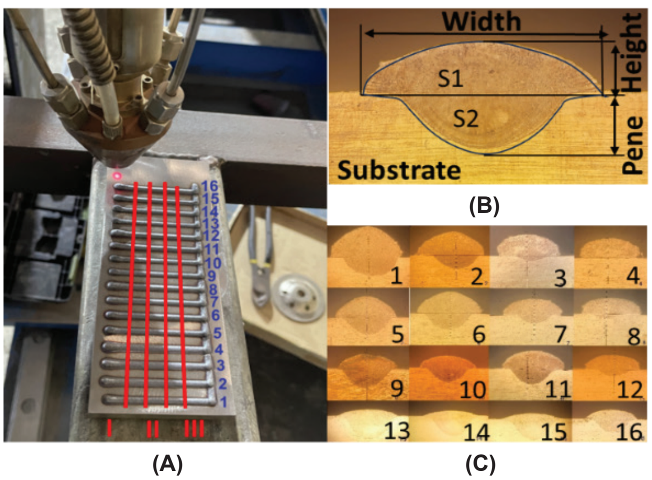


**Fig 2. (A) 16 single tracks, (B) cross-section of a single track, and (C) cross-sections of 16 single tracks.**

In the top view (Fig. 2A), 16 single tracks utilising various technological strategies demonstrate that each groove is consistent and stable. Consequently, we can assume that all these single grooves exhibit nearly uniform width and height measurements, particularly in the central area of each groove. The groove characteristics were assessed at three cross-sectional positions (I, II, III) from the midpoint of their length, which were obtained using a wire cutting machine along three predefined lines, as shown in Fig. 2A. This method mitigates the influence of edge effects and is extensively employed in prior research within the literature [11]. Accordingly, three cross-sections of each single groove in the central region were removed, ground, polished with water sandpaper ranging from 240 to 3000 grit, and chemically etched to measure the parameters. An optical microscope (AXIO A2M, Carl Zeiss) was used to determine the dimensions of the samples, including W, H, Pene and areas $S_1$ and $S_2$, as illustrated in Fig. 2B. Additionally, ImageJ software was employed to measure the dimensions of the samples, with measurements recorded at three cross-sectional locations and then averaged, as seen in Fig. 2C. The results are presented in Table 3.

One of the essential geometric characteristics is dilution, as illustrated in Fig. 2B. Dilution can be defined as follows [17]:

$$Dilution\,(\%)\ \frac{S_2}{S_1+S_2}\ \text{x } 100\% \qquad (1)$$

where $S_1$ represents the raised area above the substrate (mm$^2$) and $S_2$ represents the melted area below the substrate (mm$^2$).

The collected data were employed to examine the impact of process parameters on the characteristics of each deposited track and to design optimisation models.

**Table 3. Laser cladding matrix and responses.**

| Runs | P (W) | S (mm/min) | F (g/min) | Width (mm) | Height (mm) | Pene (mm) | S1 (mm$^2$) | S2 (mm$^2$) | Dilution (%) |
|---|---|---|---|---|---|---|---|---|---|
| 1 | 1200 | 800 | 12 | 2.969 | 1.355 | 0.821 | 2.897 | 1.328 | 31.43 |
| 2 | 1200 | 900 | 14 | 2.832 | 1.024 | 0.576 | 2.065 | 0.746 | 26.54 |
| 3 | 1200 | 1000 | 16 | 2.387 | 0.876 | 0.176 | 1.737 | 0.15 | 7.95 |
| 4 | 1200 | 1100 | 18 | 2.185 | 0.793 | 0.043 | 1.457 | 0.023 | 1.55 |
| 5 | 1500 | 800 | 14 | 2.735 | 1.035 | 0.848 | 2.05 | 1.24 | 37.69 |
| 6 | 1500 | 900 | 12 | 2.680 | 1.011 | 0.742 | 2.023 | 1.019 | 33.50 |
| 7 | 1500 | 1000 | 18 | 2.330 | 0.711 | 0.341 | 1.352 | 0.314 | 18.85 |
| 8 | 1500 | 1100 | 16 | 2.282 | 0.696 | 0.192 | 1.295 | 0.14 | 9.76 |
| 9 | 1800 | 800 | 16 | 2.667 | 0.718 | 0.920 | 1.392 | 1.339 | 49.03 |
| 10 | 1800 | 900 | 18 | 2.534 | 0.584 | 0.651 | 1.133 | 0.809 | 41.66 |
| 11 | 1800 | 1000 | 12 | 2.477 | 0.802 | 0.634 | 1.6 | 0.777 | 32.69 |
| 12 | 1800 | 1100 | 14 | 2.289 | 0.682 | 0.258 | 1.188 | 0.291 | 19.68 |
| 13 | 2100 | 800 | 18 | 2.612 | 0.303 | 1.010 | 0.542 | 1.558 | 74.19 |
| 14 | 2100 | 900 | 16 | 2.570 | 0.264 | 0.922 | 0.429 | 1.309 | 75.32 |
| 15 | 2100 | 1000 | 14 | 2.134 | 0.231 | 0.787 | 0.304 | 0.918 | 75.12 |
| 16 | 2100 | 1100 | 12 | 1.994 | 0.386 | 0.520 | 0.568 | 0.523 | 47.94 |

### 2.3. Experimental design

The purpose of this research is to determine the optimal process parameters for the SS316L cladding process. In this case, the goal is to minimise the penetration and dilution of the single deposited track while maximising its W and H. As a result, the multi-objective optimisation prompt can be described as: "Find (P, S, F) to minimise (pene and dilution) while maximising W and H." As shown in Fig. 3, the research approach is outlined to achieve these goals. To accomplish this, we conducted numerous experiments using single-geometry beads, varying the process parameter values within the limits suggested by the literature on LC for engineering alloys and high-speed LC [1, 15, 18]. After conducting several running tests, the value ranges for coating power (P), scanning speed (S), and powder feeding flow (F) were determined as follows: 1200<P (W)<2100, 800<S (mm/min)<1100, and 12<F (g/min)<18.

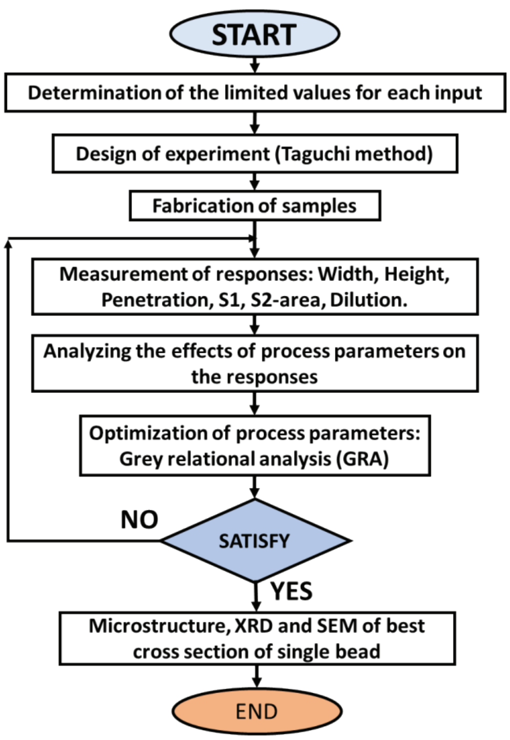


**Fig. 3. Research methodology.**

The experimental setup and sequence of steps are illustrated in Fig. 3, while the measurement results are presented in Table 3. The dilution was calculated using Equation (1).

In this study, multi-response optimisation was implemented using GRA. This method has been effectively applied across various manufacturing fields, including machining and cladding. Specifically, for the cladding process, the multi-response optimisation problem for cladding geometry beads was defined as follows [5, 6].

### 2.4. Optimisation methods: Grey relational analysis

Various strategies are employed and analysed to identify the most effective solution to the issue. The procedures utilised by the GRA are examined and briefly described as follows. GRA is a widely used approach for multi-objective optimisation in manufacturing processes [19]. This method involves converting a problem with multiple objectives into a single-objective solution. The GRA method consists of the following steps:

(1) Normalising the objective using the following criteria:

$$y_{ij}^{n} = \frac{y_{ij}^{(0)} - \min\limits_{i}\left\{y_{ij}^{(0)}\right\}}{\max\limits_{i}\left\{y_{ij}^{(0)}\right\} - \min\limits_{i}\left\{y_{ij}^{(0)}\right\}}, i=\{1,2,\ldots,m\}; j=\{1,2,\ldots,n\} \quad (2)$$

If the objective adheres to the biggest-is-best criterion.

$$y_{ij}^{(n)} = \frac{\max\limits_{i}\left\{y_{ij}^{(0)}\right\} - y_{ij}^{(0)}}{\max\limits_{i}\left\{y_{ij}^{(0)}\right\} - \min\limits_{i}\left\{y_{ij}^{(0)}\right\}}, i=\{1,2,\ldots,m\}; j=\{1,2,\ldots,n\} \quad (3)$$

If the objective adheres to the smallest-is-best criterion.

where $y_{ij}^{(0)}$ is the value of the objective measured at the trial, $\underset{i}{\mathrm{Max}}\left\{y_{ij}^{(0)}\right\}$ are the highest and $\left\{y_{ij}^{(0)}\right\}$, $\underset{i}{\mathrm{Min}}\left\{y_{ij}^{(0)}\right\}$ are the smallest values of the kth objective measured in the experiment $\left\{y_{ij}^{(0)}\right\}$, "m" is the number of test runs, and "n" is the number of responses.

(2) Calculating GRCs (Grey-relational coefficients) for normalised data using the equation:

$$\epsilon_{ij} = \frac{\delta_{\min} + \omega\delta_{\max}}{\delta_{Oi}^{(k)} + \omega\delta_{\max}} \quad (4)$$

where, $\delta_{0ij}$ is the standard deviation between the experimental values $y_{ij}^{(n)}$ and the normalised values $y_{0j}^{(n)}$, as described in the equation (5); $\delta_{min}$ and $\delta_{max}$ is the smallest and maximum of $\delta_{Oi}^{(k)}$, are calculated as equations (6) and (7); and ω is a coefficient in the range of (0,1), 0 ≤ ω ≤ 1. In this study, ω=0.5.

$$\delta_{Oij} = \left|y_{ij}^{(n)} - y_{Oj}^{(n)}\right| \quad (5)$$

$$\delta_{\min} = \min_{\forall i}\left\{\min_{\forall i}\delta_{Oij}\right\} \quad (6)$$

$$\delta_{\max} = \max_{\forall i}\left\{\max_{\forall i}\delta_{Oij}\right\} \quad (7)$$

(3) Calculating the GRGs (Grey-relational grades) by Equation :

$$\zeta_i = \sum_{j=1}^{n} w_i * \in_{ij} \quad (8)$$

where $w_i$ is the weight of objective i, $\sum_{i=1}^{n} w_i = 1$ and $0<\zeta_i<1$, and finally the optimised solution corresponds to the maximum value of $\zeta_i$.

## 3. Results and discussion

This research used Minitab 18 software to create prediction models for single-track variables, namely W, H, Pene, and dilution. The ANOVA for the models was performed at a 95% confidence level and a 5% significance level.

### *3.1. Effect of process parameter on width (mm)*

The predictive model of W is delineated by Equation (9), and the ANOVA for the model of W is shown in Table 4. that the results indicate that the model and all its terms {P, S, and F} are significant, with a P-value less than 0.05. Among the process parameters, the S contributes the most at 73.75%, followed by P at 12.20%, and F at 2.47%.

$$W(mm) = 4.51 - 0.00113P + 0.00265S - 0.171F - 0.00180F^2 - 0.000001P*S + 0.000139P*F - 0.000031S*F \quad (9)$$

*: the non-significant interaction and quadratic terms (p>0.05) have been eliminated.

Figure 4 illustrates the primary influence of process parameters on W. It indicates that as the nozzle traverse speed increases, W is significantly affected by the resulting in a rapid reduction in W per unit of deposition length. Consequently, the W of the bead geometry becomes smaller at higher traverse speeds. Similarly, W increases when P decreases; however, this relationship does not exhibit a consistent pattern. Moreover, W rises when the F decreases and often remains minimal within the design space. This finding corresponds with the ANOVA results presented in Table 4.

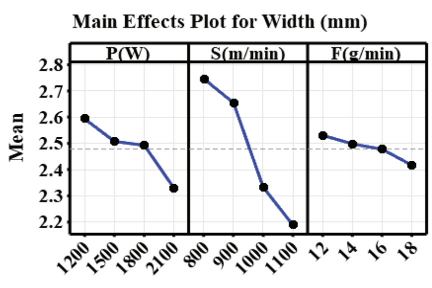


**Fig. 4. The influence of process parameters on the width of geometry bead.**

The observed pattern of S on W in the present study aligns with the findings reported in [6, 9]. An increase in S theoretically results in a decrease in the contact time of metal powder with the melting pool, thereby reducing the tack W and the deposited track W. The coefficients of determination for the model {R-sq=95.24%, R-sq (adj)=88.10%} demonstrate the significant predictive accuracy of the model. Therefore, the established equation for W can be used to accurately predict the W of each single track across the entire design space, serving as a reliable objective function for the optimisation problem.

**Table 4. ANOVA results evaluating the influence of process parameters on W (mm).**

| Source | DF | Seq SS | Contribution | Adj MS | F-value | P-value | |
|---|---|---|---|---|---|---|---|
| Regression | 9 | 1.02975 | 95.24% | 0.114417 | 13.33 | 0.003 | Significant |
| P(W) | 1 | 0.13195 | 12.20% | 0.004727 | 0.55 | 0.486 | |
| S(mm/min) | 1 | 0.79740 | 73.75% | 0.002165 | 0.25 | 0.633 | |
| F(g/min) | 1 | 0.02668 | 2.47% | 0.004215 | 0.49 | 0.510 | |
| P(W)*P(W) | 1 | 0.00605 | 0.56% | 0.006045 | 0.70 | 0.433 | |
| S(mm/min)*S(mm/min) | 1 | 0.00278 | 0.26% | 0.002783 | 0.32 | 0.590 | |
| F(g/min)*F(g/min) | 1 | 0.00083 | 0.08% | 0.000827 | 0.10 | 0.767 | |
| P(W)*S(mm/min) | 1 | 0.00248 | 0.23% | 0.002479 | 0.29 | 0.610 | |
| P(W)*F(g/min) | 1 | 0.06124 | 5.66% | 0.061239 | 7.14 | 0.037 | |
| S(mm/min)*F(g/min) | 1 | 0.00035 | 0.03% | 0.000348 | 0.04 | 0.847 | |
| Error | 6 | 0.05149 | 4.76% | 0.008581 | | | |
| Total | 15 | 1.08124 | 100.00% | | | | |
| R-sq=95.24%, R-sq(adj)=88.10% | | | | | | | |

### *3.2. Effect of process parameter to height (mm)*

Figure 5 illustrates the influence of process parameters on the H of the geometry bead. H decreases as S rises from 800 to 1100 mm/min, and height increases as P declines from 2100 to 1200 W. Similarly, H tends to increase when F decreases from 18 to 12 g/min. The trends in H variations concerning the process parameters (P, S, and F) align with the design space. The reduction in deposited track H with an increase in S and P can be attributed to the decreased powder quantity per unit length in the deposition direction as S rises. Concurrently, H increases as P diminishes. This occurs because an increase in P leads to a higher energy input, which consequently results in a larger volume of melted powder, deeper penetration, and greater dilution. As a result, a larger molten pool is generated, leading to a reduction in both the W and H of the deposited track.

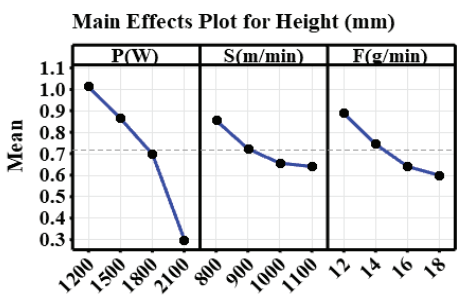


**Fig. 5. The influence of process parameters on the height of geometry bead.**

The predictive model for H is outlined in Equation (10), and the ANOVA results for this model are presented in Table 5. The results indicate that the model and all its terms {P, S, and F} exhibit P-values less than 0.05, confirming their significance. In this model, P has the highest contribution at 72.95%, while the F and S contribute 12.99 and 6.79%, respectively. The coefficients of determination for the model {R-sq=98.94%, R-sq(adj)=97.35%} demonstrate a high degree of predictive accuracy. This model can reliably estimate the H of single tracks across the design space and may serve as an objective function for the optimisation problem.

$$H\left(mm\right) = 6.42+0.000758P - 0.00670S - 0.251F + 0.00655F*F + 0.000001P*S + 0.000018P*F - 0.000018S*F \quad (10)$$

*: the non-significant interaction and quadratic terms (p>0.05) have been eliminated.

**Table 5. ANOVA results evaluating the influence of process parameters on H (mm).**

| Source | DF | Seq SS | Contribution | Adj MS | F-value | P-value | |
|---|---|---|---|---|---|---|---|
| Regression | 9 | 1.45335 | 98.94% | 0.161483 | 62.34 | 0.000 | Significant |
| P(W) | 1 | 1.07161 | 72.95% | 0.002126 | 0.82 | 0.400 | |
| S(mm/min) | 1 | 0.09976 | 6.79% | 0.013813 | 5.33 | 0.060 | |
| F(g/min) | 1 | 0.19081 | 12.99% | 0.009056 | 3.50 | 0.111 | |
| P(W)*P(W) | 1 | 0.06338 | 4.31% | 0.063378 | 24.47 | 0.003 | |
| S(mm/min)*S(mm/min) | 1 | 0.01351 | 0.92% | 0.013514 | 5.22 | 0.062 | |
| F(g/min)*F(g/min) | 1 | 0.01097 | 0.75% | 0.010973 | 4.24 | 0.085 | |
| P(W)*S(mm/min) | 1 | 0.00210 | 0.14% | 0.002105 | 0.81 | 0.402 | |
| P(W)*F(g/min) | 1 | 0.00108 | 0.07% | 0.001080 | 0.42 | 0.542 | |
| S(mm/min)*F(g/min) | 1 | 0.00012 | 0.01% | 0.000119 | 0.05 | 0.838 | |
| Error | 6 | 0.01554 | 1.06% | 0.002590 | | | |
| Total | 15 | 1.46889 | 100.00% | | | | |
| R-sq=98.94%, R-sq(adj)=97.35% | | | | | | | |

### *3.3. Effect of process parameters on penetration (mm)*

Figure 6 presents the influence of process parameters on the Pene of a single track. The Pene depth increases with an increase in laser power, rising from 1200 to 2100 W. Conversely, Pene decreases as the scanning speed rises from 800 to 1100 mm/min and as the powder feed rate increases from 12 to 18 g/min. Previous studies have shown a similar tendency regarding the effects of P, S, and F on Pene [9]. As previously mentioned, an increase in P, coupled with a decrease in the powder feed rate, results in a greater amount of laser energy being applied to the material during deposition. This produces a more pronounced localised heating effect, leading to deeper penetration. Moreover, an increased scanning velocity diminishes the contact duration between the laser and the substrate, thereby constraining energy absorption and consequently decreasing penetration.

The penetration prediction model is presented in Equation (11), and the ANOVA results for the penetration model are shown in Table 6. The model and all its parameters {P, S, F} are significant, with P-values below 0.05. The S has the greatest contribution at 68.27%, followed by P and F, which contribute 24.41 and 4.66%, respectively. The determination coefficients of the model {R-sq=98.99%, R-sq(adj)=97.45%} validate that the constructed model of Pene exhibits high predictive accuracy. This model may be used to forecast the penetration of individual tracks throughout the entire design space and can be applied to the optimisation problem.

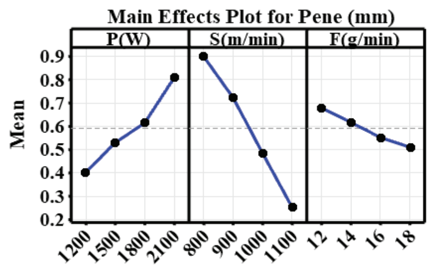


**Fig. 6. The influence of process parameters on the Pene of geometry bead.**

$$Pene\left(mm\right) = 4.06+0.000310P-0.00208S-0.254F-0.00130F*F-0.0002S*F \quad (11)$$

*: the non-significant interaction and quadratic terms (p>0.05) have been eliminated.

**Table 6. ANOVA results evaluating the influence of process parameters on P (mm).**

| Source | DF | Seq SS | Contribution | Adj MS | F-value | P-value | |
|---|---|---|---|---|---|---|---|
| Regression | 9 | 1.37519 | 98.98% | 0.152799 | 64.77 | 0.000 | Significant |
| P(W) | 1 | 0.33917 | 24.41% | 0.000354 | 0.15 | 0.712 | |
| S(mm/min) | 1 | 0.94852 | 68.27% | 0.001335 | 0.57 | 0.480 | |
| F(g/min) | 1 | 0.06470 | 4.66% | 0.009268 | 3.93 | 0.095 | |
| P(W)*P(W) | 1 | 0.00452 | 0.33% | 0.004523 | 1.92 | 0.215 | |
| S(mm/min)*S(mm/min) | 1 | 0.00294 | 0.21% | 0.002943 | 1.25 | 0.307 | |
| F(mg/s)*F(g/min) | 1 | 0.00043 | 0.03% | 0.000431 | 0.18 | 0.684 | |
| P(W)*S(mm/min) | 1 | 0.00083 | 0.06% | 0.000831 | 0.35 | 0.575 | |
| P(W)*F(g/min) | 1 | 0.00006 | 0.00% | 0.000059 | 0.02 | 0.880 | |
| S(mm/min)*F(g/min) | 1 | 0.01402 | 1.01% | 0.014024 | 5.94 | 0.051 | |
| Error | 6 | 0.01415 | 1.02% | 0.002359 | | | |
| Total | 15 | 1.38935 | 100.00% | | | | |
| R-sq=98.99%, R-sq(adj)=97.45%, and R-sq(pred)=93.31% | | | | | | | |

### *3.4. Effect of process parameter to dilution*

Dilution markedly increases with a rise in P, going from 1200 to 2100 W. Conversely, dilution decreases as S rises from 800 to 1100 mm/min, while F has a slightly smaller but still diminishing impact on dilution as it increases from 12 to 18 g/min. The prediction model for dilution is represented by Equation (12), and the ANOVA results for the dilution model are presented in Table 7. The results indicate that the model and all its terms {P, S, F} are significant, with P-values below 0.05. Fig. 7 illustrates the direct impacts of process factors on the dilution of the deposited track.

**Table 7. ANOVA results evaluating the influence of process parameters on dilution.**

| Source | DF | Seq SS | Contribution | Adj MS | F-value | P-value | |
|---|---|---|---|---|---|---|---|
| Regression | 9 | 8126.47 | 98.75% | 902.942 | 52.58 | 0.000 | Significant |
| P(W) | 1 | 5420.95 | 65.87% | 99.852 | 5.82 | 0.052 | |
| S(mm/min) | 1 | 1830.35 | 22.24% | 1.866 | 0.11 | 0.753 | |
| F(g/min) | 1 | 25.19 | 0.31% | 14.410 | 0.84 | 0.395 | |
| P(W)*P(W) | 1 | 590.47 | 7.18% | 590.470 | 34.39 | 0.001 | |
| S(mm/min)*S(mm/min) | 1 | 101.77 | 1.24% | 101.774 | 5.93 | 0.051 | |
| F(g/min)*F(g/min) | 1 | 23.21 | 0.28% | 23.214 | 1.35 | 0.289 | |
| P(W)*S(mm/min) | 1 | 0.50 | 0.01% | 0.504 | 0.03 | 0.870 | |
| P(W)*F(g/min) | 1 | 0.01 | 0.00% | 0.006 | 0.00 | 0.986 | |
| S(mm/min)*F(g/min) | 1 | 134.01 | 1.63% | 134.009 | 7.80 | 0.031 | |
| Error | 6 | 103.03 | 1.25% | 17.171 | | | |
| Total | 15 | 8229.50 | 100.00% | | | | |
| R-sq=98.75%, R-sq(adj)=96.87%, and R-sq(pred) =88.43% | | | | | | | |

P has the greatest contribution at 65.87%, followed by S at 22.24% and F at 0.31%. The effect trend of these variables on dilution is inconsistent. The determination coefficients of the model {R-sq=98.75%, R-sq(adj)=96.87%} indicate that the developed model for dilution exhibits high predictive accuracy. A similar observation regarding the effects of P, S, F on dilution has been reported in previous studies [4, 6, 15]. This model may be used to forecast the dilution of single tracks across the entire design space and can facilitate optimisation.

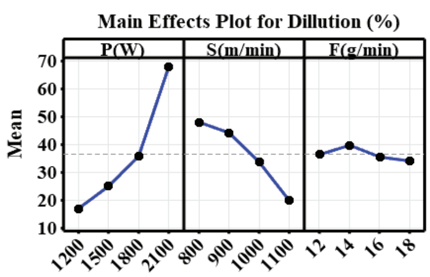


**Fig. 7. The influence of process parameters on the dilution of geometry bead.**

$$Dilution\left(\%\right) = 201 - 0.1644P + 0.078S - 10.0F - 0.301F*F + 0.01951S*F \quad (12)$$

*: the non-significant interaction and quadratic terms (p>0.05) have been eliminated.

### *3.5. Optimisation results: Grey relational analysis results*

Table 8 presents the results calculated using the GRA method, in which the normalised responses were determined using Equation (2) for the values of W and H and Equation (3) for the values of Pene and dilution. The values of the GRC are calculated using Equation (5), and finally, the values of the GRG are derived from Equation (8). Based on the GRG values, the rankings for all alternatives are given in the ranking column of Table 8. Experiment No. 1, which has the highest GRG value, is considered the optimal condition. Therefore, the set of process parameters associated with experiment No. 1 represents the optimal combination of process parameters.

**Table 8. Results of the normalisation of responses, GRC, GRG, and rankings.**

| Run | Normalised response | | | | GRC | | | | GRG | Rank |
|---|---|---|---|---|---|---|---|---|---|---|
| | *W* | *H* | *P* | *D* | *W* | *H* | *P* | *D* | | |
| 1 | 1.000 | 1.000 | 0.195 | 0.595 | 1.000 | 1.000 | 0.383 | 0.552 | 0.7339 | 1 |
| 2 | 0.859 | 0.706 | 0.449 | 0.661 | 0.781 | 0.629 | 0.476 | 0.596 | 0.6204 | 4 |
| 3 | 0.403 | 0.574 | 0.862 | 0.913 | 0.456 | 0.540 | 0.784 | 0.852 | 0.6580 | 3 |
| 4 | 0.196 | 0.500 | 1.000 | 1.000 | 0.383 | 0.500 | 1.000 | 1.000 | 0.7209 | 2 |
| 5 | 0.760 | 0.715 | 0.168 | 0.510 | 0.676 | 0.637 | 0.375 | 0.505 | 0.5483 | 8 |
| 6 | 0.704 | 0.694 | 0.277 | 0.567 | 0.628 | 0.620 | 0.409 | 0.536 | 0.5482 | 9 |
| 7 | 0.345 | 0.427 | 0.692 | 0.766 | 0.433 | 0.466 | 0.619 | 0.681 | 0.5496 | 7 |
| 8 | 0.295 | 0.414 | 0.846 | 0.889 | 0.415 | 0.460 | 0.764 | 0.818 | 0.6145 | 5 |
| 9 | 0.690 | 0.433 | 0.093 | 0.356 | 0.617 | 0.469 | 0.355 | 0.437 | 0.4697 | 11 |
| 10 | 0.554 | 0.314 | 0.371 | 0.456 | 0.528 | 0.422 | 0.443 | 0.479 | 0.4680 | 12 |
| 11 | 0.495 | 0.508 | 0.389 | 0.578 | 0.498 | 0.504 | 0.450 | 0.542 | 0.4985 | 10 |
| 12 | 0.303 | 0.401 | 0.778 | 0.754 | 0.418 | 0.455 | 0.692 | 0.671 | 0.5588 | 6 |
| 13 | 0.634 | 0.064 | 0.000 | 0.015 | 0.577 | 0.348 | 0.333 | 0.337 | 0.3989 | 14 |
| 14 | 0.591 | 0.029 | 0.091 | 0.000 | 0.550 | 0.340 | 0.355 | 0.333 | 0.3945 | 15 |
| 15 | 0.144 | 0.000 | 0.231 | 0.003 | 0.369 | 0.333 | 0.394 | 0.334 | 0.3574 | 16 |
| 16 | 0.000 | 0.138 | 0.507 | 0.371 | 0.333 | 0.367 | 0.503 | 0.443 | 0.4117 | 13 |

### *3.6. X-ray diffraction, scanning electron microscopy and hardness of sample No.1*

*XRD:* The XRD spectrum of the typical single clad layer from Experiment 1 is presented in Fig. 8. The major peaks in the spectrum were observed at 2Θ=43.5, 50.70, and 74.6°, which correspond to the characteristic crystallographic planes of the austenitic phase (γ-Fe). The strong peaks further confirm the dominant presence of the FCC austenite structure. Additionally, weaker peaks suggest the existence of secondary phases, possibly due to a small amount of δ-ferrite (BCC phase). These results are consistent with those of a previous study [20]. The amalgamation of austenite and δ-ferrite enhances mechanical properties, yielding superior ductility, improved wear resistance, and increased resistance to hot cracking, thereby making the laser-cladded stainless steel SS316L suitable for high-performance applications.

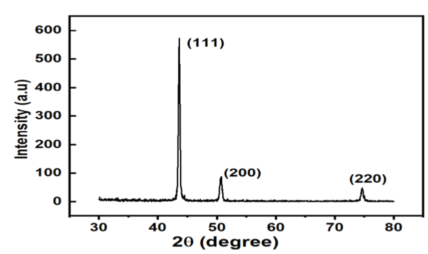


**Fig. 8. XRD of cross section clad bead 316L.**

The pronounced intensity of the (111) peak indicates a preferred crystallographic orientation, evidencing texture development during rapid solidification. This texture evolution, driven by the steep thermal gradients characteristic of LC, stabilises γ-austenite with minimal δ-ferrite, thereby improving mechanical reliability.

*SEM:* Fig. 9 illustrates the microstructure of the cross-section of sample No. 1, fabricated with a P of 1200 W, a S of 800 mm/min, and a F of 12 g/min. It demonstrates an effective metallurgical bond between the base material and the deposited layer, devoid of visible detachment or significant voids; similar results were observed in a previous study [12].

Table 9 presents the EDS analysis of the laser-cladded SS316L, indicating that the main alloying elements (Cr, Ni, Mo) are preserved, thereby ensuring corrosion resistance and mechanical stability. Regions A and B display a composition similar to that of SS316L powder, with Cr (~17.08-17.60 wt.%), Mo (~1.31-1.42 wt.%), and Ni (~9.18-9.47 wt.%), which enhance pitting resistance and austenitic stability. At Position C (substrate), Cr, Mo, and Ni contents are slightly lower, these alloying elements are still retained, reflecting local compositional variation within the SS316L material system rather than a significant compositional deviation, the inclusion of Si and Mn enhances oxidation resistance and toughness. The composition distribution validates the effectiveness of the LC technique, guaranteeing wear and oxidation resistance while preserving the essential features of SS316L.

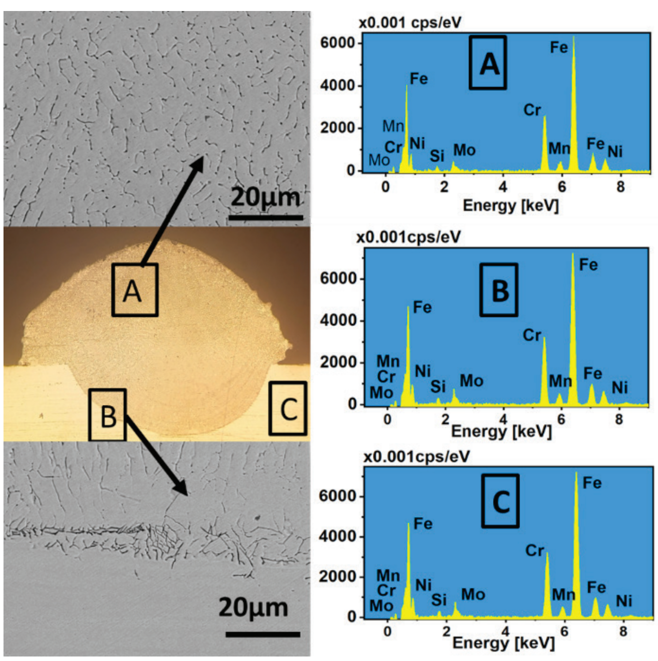


**Fig. 9. SEM images (left) and EDS elemental spectra (right) of different regions in the coating.**

**Table 9. The chemical composition at locations A, B, and C (wt.%).**

| Position | Cr (wt.%) | Mo (wt.%) | Ni (wt.%) | Si (wt.%) | Mn (wt.%) | Fe (wt.%) |
|---|---|---|---|---|---|---|
| A | 17.08 | 1.31 | 9.47 | 0.91 | 0.67 | Bal. |
| B | 17.60 | 1.42 | 9.18 | 1.17 | 0.75 | Bal. |
| C | 16.69 | 0.85 | 8.67 | 0.66 | 0.78 | Bal. |

*Microhardness:* Fig. 10 shows that the microhardness measurements in the given chart demonstrate a gradual increasing trend, ranging from 197 to 224 HV. This result has been corroborated in previous studies [11, 12], with slight fluctuations observed from the substrate (position C) to the interface layer (position B). Following an initial rise, a slight decrease at position 3 (201 HV) is likely attributable to localised microstructural differences or may result from heat accumulation in the substrate. The highest values (223-224 HV) at position A indicate a stable and refined surface layer, possibly resulting from rapid cooling, grain refinement, or phase transitions during processing. The Vickers indentation images reveal uniform deformation without significant cracks, suggesting good structural integrity. The observed pattern of increased hardness corresponds closely with the chemical composition data presented in Table 9, indicating that elevated levels of Cr, Mo, and Ni in the cladding layer enhance solid solution strengthening and wear resistance. In contrast, the lower hardness values at the substrate (position C) correlate with elevated Fe content and decreased amounts of Cr and Mo. These results indicate that maintaining essential alloying elements in the cladding layer significantly improves mechanical characteristics, leading to enhanced hardness, wear resistance, and structural stability.

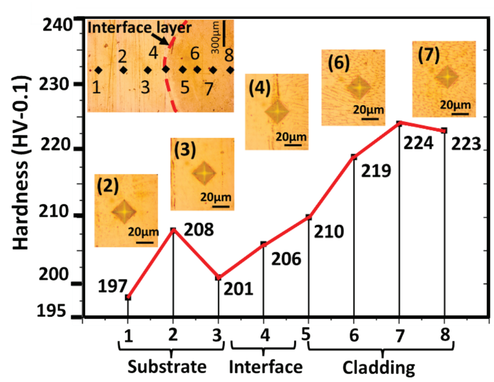


**Fig. 10. Microhardness of the cross-section of sample No. 1.**

## 4. Conclusions

This research examines the impacts of primary process factors, including P, deposition nozzle S, and F, on the characteristics of single deposited tracks and identifies the optimal process parameters for SS316L deposition while addressing multiple optimisation objectives.

P was identified as the dominant factor influencing track H and dilution, whereas S was the primary factor affecting deposited track W and significantly influenced Pene; in contrast, the influence of F was relatively minor.

The predictive models for bead geometry achieved high accuracy ($R^2$>95%), confirming their reliability for process prediction. Multi-response optimisation using GRA identified the optimal parameters (P=1200 W, S=800 mm/min, F=12 g/min), which produced coatings with a stable austenitic FCC structure, increased hardness from substrate to cladding, and improved mechanical performance resulting from grain refinement and compositional stability.

Overall, the findings offer useful guidance for enhancing LC efficiency and support process control in industrial applications. Future research should focus on improving corrosion resistance, developing multi-layer deposition strategies, and exploring alternative alloying approaches to enhance durability in demanding environments.

## CRediT author statement

Van Quan Nguyen: Formal analysis, Methodology, Designing the analysis, Collecting data, Writing-original draft preparation; Tat Khoa Doan: Methodology, Supervision, Reviewing and Editing; Van Nguy Duong: Methodology, Designing the analysis; Van Hoang Nguyen: Methodology, Supervision, Reviewing and Editing.

## COMPETING INTERESTS

The authors declare that there is no conflict of interest regarding the publication of this article.

## REFERENCES


[1] L. Zhu, X.S. Peng, L. Qing, et al. (2021), "Recent research and development status of laser cladding: A review", *Optics & Laser Technology*, **138**, DOI: 10.1016/j.optlastec.2021.106915.

[2] Y. Liu, Y. Ding, L. Yang, et al. (2021), "Research and progress of laser cladding on engineering alloys: A review", *Journal of Manufacturing Processes*, **66**, pp.341-363, DOI: 10.1016/j.jmapro.2021.03.061.

[3] G. Meng, L. Zhu, J. Zhang, et al. (2021), "Statistical analysis and multi-objective process optimization of laser cladding TiC-Inconel718 composite coating", *Optik*, **240**, DOI: 10.1016/j.ijleo.2021.166828.

[4] Y. Javid (2020), "Multi-response optimization in laser cladding process of WC powder on Inconel 718", *CIRP Journal of Manufacturing Science & Technology*, **31**, pp.406-417, DOI: 10.1016/j.cirpj.2020.07.003.

[5] T. Yu, L. Yang, Y. Zhao, et al. (2018), "Experimental research and multi-response multi-parameter optimization of laser cladding Fe313", *Optics & Laser Technology*, **108**, pp.321-332, DOI: 10.1016/j.optlastec.2018.06.030.

[6] Y. Du, G. He, Z. Zhou, et al. (2023), "Multi-objective optimization of process parameters of laser cladding 15-5PH alloy powder based on gray-fuzzy taguchi approach", *Engineering Research Express*, **5(2)**, DOI: 10.1088/2631-8695/acc9fe.

[7] A. Solati, N.B.M. Arab, A.M. Ahmar, et al. (2018), "Multi-criteria optimization of weld bead in pulsed Nd:YAG laser welding of stainless steel 316", *Proceedings of The Institution of Mechanical Engineers, Part E: Journal of Process Mechanical Engineering*, **233(2)**, pp.151-164, DOI: 10.1177/0954408918756654.

[8] Y.Y. Chang, J.R. Qiu, S.J. Hwang (2022), "Multi-objective optimization of directed energy deposition process by using Taguchi-Grey relational analysis", *International Journal of Advanced Manufacturing Technology*, **120**, pp.7547-7563, DOI: 10.1007/s00170-022-09210-3.

[9] K.D. Tat, V.T. Le, N.D. Van (2024), "Prediction models and multi-objective optimization of the single deposited tracks in laser direct metal deposition of 316L stainless steel", *Manufacturing Review (Les Ulis)*, **11,** DOI: 10.1051/mfreview/2024012.

[10] X. Li, T. Li, B. Shi, et al. (2020), "The influence of substrate tilt angle on the morphology of laser cladding layer", *Surface and Coatings Technology*, **391**, DOI: 10.1016/j.surfcoat.2020.125706.

[11] H. Ding, Y. Tao, W. Wenjian, et al. (2023), "Optimization and wear behaviors of 316L stainless steel laser cladding on rail material", *Wear*, **523**, DOI: 10.1016/j.wear.2023.204830.

[12] E.R.I. Mahmoud, S.Z. Khan, M. Ejaz (2021), "Laser surface cladding of mild steel with 316L stainless steel for anti-corrosion applications", *Materials Today: Proceedings*, **18**, pp.1029-1033, DOI: 10.1016/j.matpr.2020.04.763.

[13] A. Fathi, E. Toyserkani, A. Khajepour, et al. (2006), "Prediction of melt pool depth and dilution in laser powder deposition", *Journal of Physics D: Applied Physics*, **39(12)**, pp.2613-2623, DOI: 10.1088/0022-3727/39/12/022.

[14] J. Hao, Q. Meng, C. Li, et al. (2019), "Effects of tilt angle between laser nozzle and substrate on bead morphology in multi-axis laser cladding", *Journal of Manufacturing Processes*, **43**, pp.311-322, DOI: 10.1016/j.jmapro.2019.04.025.

[15] Y. Liang, Z.Y. Liao, L.L. Zhang, et al. (2023), "A review on coatings deposited by extreme high-speed laser cladding: Processes, materials, and properties", *Optics & Laser Technology*, **164**, DOI: 10.1016/j.optlastec.2023.109472.

[16] P.J. DePond, G. Gabe, L. Sonny, et al. (2018), "In situ measurements of layer roughness during laser powder bed fusion additive manufacturing using low coherence scanning interferometry", *Materials & Design*, **154**, pp.347-359, DOI: 10.1016/j.matdes.2018.05.050.

[17] J. Liu, J. Li, X. Cheng, et al. (2017), "Effect of dilution and macrosegregation on corrosion resistance of laser clad AerMet100 steel coating on 300M steel substrate", *Surface and Coatings Technology*, **325**, pp.352-359, DOI: 10.1016/j.surfcoat.2017.04.035.

[18] L. Zhou, G.Z. Ma, H.C. Zhao, et al. (2024), "Research status and prospect of extreme high-speed laser cladding technology", *Optics & Laser Technology*, **168**, DOI: 10.1016/j.optlastec.2023.109800.

[19] D. Deng, T. Li, Z. Huang, et al. (2022), "Multi-response optimization of laser cladding for TiC particle reinforced Fe matrix composite based on Taguchi method and grey relational analysis", *Optics & Laser Technology*, **153**, DOI: 10.1016/j.optlastec.2022.108259.

[20] Z. Chen, W. Sun, Y. Huang, et al. (2022), "The effect of laser energy density on microstructural evolution and mechanical properties of laser clad 316L stainless steel for repair", *Surface and Coatings Technology*, **448**, DOI: 10.1016/j.surfcoat.2022.128899.